Katabatically Driven Cold Air Intrusions into a Basin Atmosphere

C. DAVID WHITEMAN, MANUELA LEHNER,[a] AND SEBASTIAN W. HOCH

University of Utah, Salt Lake City, Utah

BIANCA ADLER AND NORBERT KALTHOFF

Karlsruhe Institute of Technology, Karlsruhe, Germany

THOMAS HAIDEN

European Centre for Medium-Range Weather Forecasting, Reading, United Kingdom

(Manuscript received 9 May 2017, in final form 11 October 2017)

ABSTRACT

The interactions between a katabatic flow on a plain and a circular basin cut into the plain and surrounded by an elevated rim were examined during a 5-h steady-state period during the Second Meteor Crater Experiment (METCRAX II) to explain observed disturbances to the nocturnal basin atmosphere. The approaching katabatic flow split horizontally around Arizona's Meteor Crater below a dividing streamline while, above the dividing streamline, an ~50-m-deep stable layer on the plain was carried over the 30–50-m rim of the basin. A flow bifurcation occurred over or just upwind of the rim, with the lowest portion of the stable layer having negative buoyancy relative to the air within the crater pouring continuously over the crater's upwind rim and accelerating down the inner sidewall. The cold air intrusion was deepest and coldest over the direct upwind crater rim. Cold air penetration depths varied around the inner sidewall depending on the temperature deficit of the inflow relative to the ambient environment inside the crater. A shallow but extremely stable cold pool on the crater floor could not generally be penetrated by the inflow and a hydraulic jump–like feature formed on the lower sidewall as the flow approached the cold pool. The upper non-negatively buoyant portion of the stable layer was carried horizontally over the crater, forming a neutrally stratified, low–wind speed cavity or wake in the lee of the upwind rim that extended downward into the crater over the upwind sidewall.

1. Introduction

Currents of cold air on scales ranging from microscale to synoptic scale have often been observed to flow over topographic obstacles (Seemann 1979; Orr et al. 2008). These flows descend the lee slope when they have negative buoyancy relative to air in the lee of the obstacle. In contrast to thermally driven downslope winds that are an iconic feature of mountain meteorology and are driven by a local negative energy budget on the slope (Zardi and Whiteman 2012), these downslope currents are driven by a continuous overflow of cold air at the top of the slope. The overflow can sometimes be visualized by the presence of a stratiform cloud layer that spills over a ridge and dissipates as cloud droplets evaporate in the descending air. In clear air, the presence of a cold airstream or intrusion is often recognized by strong and gusty winds on the lee slope. On mountains with significant topographic relief the cold air descent in the lee of the mountains becomes strong and turbulent as, for example, in bora windstorms on the Adriatic coast (Grisogono and Belušić 2009).

In the present study, we investigate a synoptically undisturbed thermally driven katabatic flow on a mesoscale plain that is approaching the elevated rim of a small circular crater basin, with the goal of determining the characteristics of the approaching flow, the disturbance to this flow caused by the crater, and the impact on atmospheric structure inside and above the crater as

Supplemental information related to this paper is available at the Journals Online website: https://doi.org/10.1175/JAMC-D-17-0131.s1.

[a] Current affiliation: University of Innsbruck, Innsbruck, Austria.

Corresponding author: C. David Whiteman, dave.whiteman@utah.edu

DOI: 10.1175/JAMC-D-17-0131.1

the cold katabatically driven air mass is carried over the crater rim. The compact Meteor Crater (Arizona) topography allows the various thermally and dynamically driven phenomena to be investigated using an extensive dataset from a variety of surface-based in situ and remote sensing instruments. The knowledge of these phenomena is expected to be of widespread generality and practicality, as dense fluid flows over topography are ubiquitous in nature, being present not only in the atmosphere but also in lacustrine (Thorpe 1998) and oceanic environments (Armi and Farmer 2002).

2. Background

The First Meteor Crater Experiment (METCRAX; Whiteman et al. 2008) of October 2006 investigated the formation of nocturnal stable boundary layers in the topographically simple Barringer Meteor Crater basin. An unusual isothermal temperature structure was found in the upper 75%–80% of the basin, and conceptual (Whiteman et al. 2010), analytical (Haiden et al. 2011), and numerical (Kiefer and Zhong 2011) models attributed the isothermalcy to katabatically driven cold air intrusions over the upwind rim. A second Meteor Crater Experiment (METCRAX II) in October 2013 (Lehner et al. 2016b) greatly expanded the observational network to better study the cold air intrusions and to follow up on the serendipitous discovery of occasional warm air intrusions (Adler et al. 2012) that led to downslope windstorm-type flows on the crater sidewalls. For the cold air intrusions, the new observations allowed simultaneous investigations of the nocturnal mesoscale katabatic flow on the plain upwind of the crater; its interaction with the crater rim, including the flow splitting around the crater and the lifting of cold air over the rim; the descent and acceleration of cold air into the crater basin; and the formation of a hydraulic jump–like feature on the lower sidewall, topics of the present paper.

The combination of these phenomena affecting the Meteor Crater basin has not, to our knowledge, been investigated elsewhere, but some individual components have received previous study. Thermally driven katabatic flows on inclined slopes have been well studied (e.g., Poulos and Zhong 2008; Zardi and Whiteman 2012). And Savage et al.'s (2008) numerical simulations of the katabatic flow on the plain outside the crater were in general agreement with limited METCRAX observations.

An extensive scientific literature covers flows of stably stratified fluids over hills and mountains (e.g., Smith 1989; Baines 1995; Vosper et al. 1999; Reinecke and Durran 2008). Flow over the 30–50-m-high crater rim is at the lower topographic limit of such studies. Continuous flows into topographic basins have received much less research attention than flows over topographic obstacles. Theoretical and numerical studies, motivated by observations from the Meteor Crater, have been recently published (Lehner et al. 2016a; Rotunno and Lehner 2016). These studies investigated various nondimensional characteristics of the approaching flow and topography to show a variety of flow responses to basin topography, including overflow, flow separations, single or multiple waves in the lee of the upwind basin edge, hydraulic flows, and hydraulic jumps. Continuous natural cold air inflows at the tops of slopes appear not to have been studied. There are, however, laboratory analog experiments in which a continuous flow of a dense fluid is introduced into a stably stratified fluid (Baines 1995, 1999). In these simulations the dense fluid comes part way down into the stratified fluid and detrains from the slope into the ambient atmosphere.

Atmospheric-analog hydraulic jumps are layer flow transitions from supercritical to subcritical velocities accompanied by strongly rising isentropes and attendant loss of energy. These are sometimes seen in flows over terrain obstacles or down inclined topography. They have received little research attention in natural atmospheric environments because of their turbulent nature, their rapid changes in space and time, and the absence of detailed observations. Hydraulic jumps are known to occur, for example, on the coast of Antarctica (e.g., Renfrew 2004) where katabatic flows cascade over terrain.

3. The experimental setup

Arizona's Meteor Crater (Fig. 1) is a 170-m-deep circular basin of 1.2-km diameter with a rim extending 30–50 m above the surrounding plain. The rim height varies around the crater periphery (Fig. 2) but has no major gaps or passes that communicate directly out onto the plain. The extensive plain (part of the Colorado Plateau) is tilted upward toward the southwest of the crater at an angle of about 1°. Sidewall slope angles within the crater vary with elevation, with steep upper sidewalls (~35° slopes) transitioning to 0° at the basin floor center.

Lehner et al. (2016b) provided a full description of the METCRAX II instrumentation, measurements, and locations. Figure 1 shows the instruments and locations used in this paper. Instrumentation included lines of temperature dataloggers (Onset Computer Corp. HOBO U23 Pro v1 and v2) running up the northeast (NE), southeast (SE), south-southwest (SSW), southwest (SW), and west (W) inner sidewalls of the crater and out onto the adjacent plain, with sensors exposed at

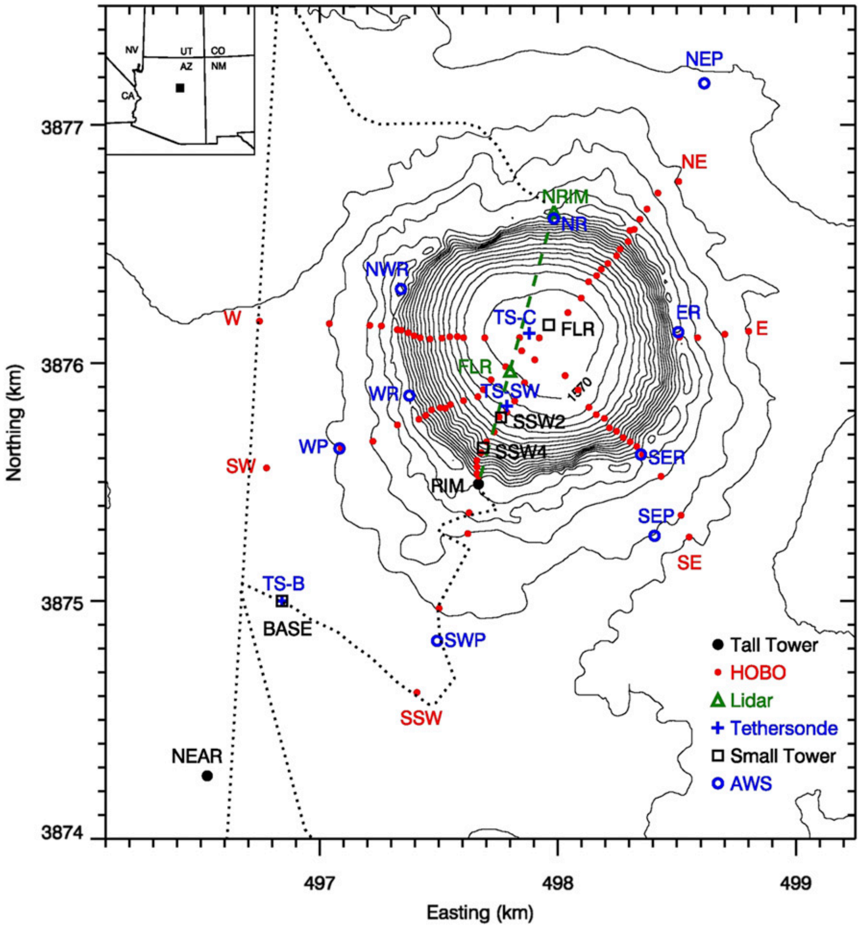

FIG. 1. Universal transverse Mercator zone 12S projection of the Meteor Crater showing the topography (10-m contours) and measurement sites. The black dotted lines are roads. The dashed green line is the axis of the vertical lidar cross section. The inset map shows the location of Meteor Crater in Arizona in the southwestern United States.

1.2 m above ground level (AGL) in radiation shields. Rim HOBOs on each of the lines are designated by the line name followed by a prime. For example, the rim HOBO on the SSW line is SSW′. Temperatures were sampled instantaneously every 2.5 min. The HOBO temperature sensors have a time constant of about 2 min and an accuracy of ±0.26°C (Whiteman et al. 2000). Where possible, HOBOs were placed at the same elevations on all lines with the height intervals between sensors increasing with distance up the sidewalls. Vertical profiles of temperature, humidity, and winds were measured continuously at 5-m height intervals on the 40-m RIM tower on the crater's south-southwest rim and on the 50-m NEAR tower southwest (upwind) of the crater. The 3-m level was substituted for the 5-m level on the NEAR tower. Tower winds were measured with three-dimensional sonic anemometers; two additional sonic anemometers were mounted on towers on the SSW sidewall at SSW2 and SSW4. Tethersondes measured profiles of temperature, relative humidity, and winds at approximately 20-min intervals during the night from the crater floor center (TS-C), the lower southwest sidewall (TS-SW), and the BASE site (TS-B) on the plain outside the crater. Ten-meter towers were placed on the crater floor (FLR) and at BASE. Automatic weather stations (AWSs) were operated on the crater's rim and on the adjacent plain to measure temperature, relative humidity, wind velocity, and wind direction.

All data except for the tethered balloon soundings were averaged to 5 min unless otherwise noted, with averages denoted by the ending times. Astronomical sunset was at 1734 mountain standard time (MST). All temperatures (T, °C) were converted to potential temperatures (θ, °C) using the formula $\theta = T + 0.0098(z - z_{\mathrm{FLR}})$, where z is elevation (m MSL), $z_{\mathrm{FLR}} = 1564$ m MSL is the crater floor elevation used as the reference level, and

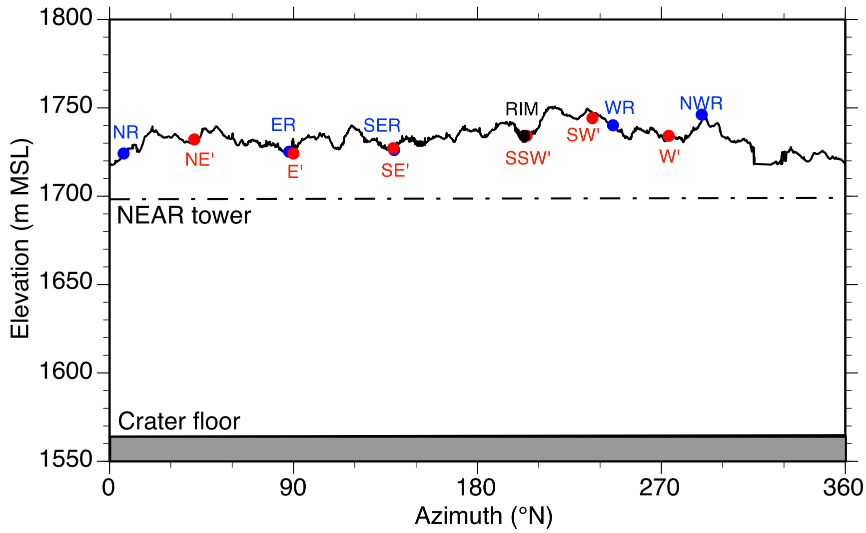

FIG. 2. Crater rim elevation vs azimuth angle from the center of the crater floor. Also shown are the elevations of the crater floor and NEAR tower (solid and dot–dashed horizontal lines, respectively), the rim tower (RIM), the AWSs (NR, ER, SER, WR, and NWR) on the crater rim, and the HOBOs on the rim for each of the HOBO lines (NE′, E′, SE′, SSW′, SW′, and W′).

$0.0098°\mathrm{C\,m^{-1}}$ is the dry adiabatic temperature gradient. While potential temperatures are reported in degrees Celsius, to avoid confusion we report potential temperature differences, gradients, and rates of change in kelvin units.

Data in this paper come primarily from the clear night of 26–27 October 2013 [intensive observational period 7 (IOP7)], with a focus on the 2300–0400 MST period when the wind direction of the katabatic flow at the NEAR tower on the tilted plain reached a near–steady state. Our experience from METCRAX and METCRAX II is that a quiescent background flow above the southwesterly katabatic flow, as on this night, is rather unusual, although two such IOPs occurred in the combined 14 IOPs of METCRAX and METCRAX II. The idealized circular crater topography, the steady-state flow, the clear night undisturbed by larger synoptic-scale flows, and the extensive dataset make IOP7 a good candidate for future testing of numerical models.

4. The approaching flow

a. *Vertical structure of the katabatic layer on the plain and at the crater rim*

Potential temperature and wind profile shapes (Fig. 3) on the plain at the NEAR tower for the near-steady-state period are typical of katabatic flows (Zardi and Whiteman 2012). The katabatic flow, however, develops on an extensive low angle plain, resulting in a higher (1725 m MSL or 28 m AGL) and stronger ($4.5–6\,\mathrm{m\,s^{-1}}$) downslope wind maximum than reported previously for steeper slopes (Horst and Doran 1986; Doran et al. 1990; Grachev et al. 2016). A low-angle (1.6°) slope on the floor of Utah's Salt Lake Valley produced similar jet-maximum speeds ($3.5–5.5\,\mathrm{m\,s^{-1}}$), but they occurred at 10–15 m AGL (Haiden and Whiteman 2005; Whiteman and Zhong 2008). The statically stable katabatic layer on the plain outside Meteor Crater extended from the surface to near or just above the top of the 50-m NEAR tower (Fig. 3a) and cooled continuously throughout the 2300–0400 MST period at the rate of about $0.6\,\mathrm{K\,h^{-1}}$. During this period the potential temperature differences between the 50- and 3-m tower levels changed from 9 to 6 K and the mean potential temperature gradient changed from 0.20 to $0.13\,\mathrm{K\,m^{-1}}$. Wind directions in the katabatic flow (Fig. 3c) veered with height from south-southwest to west-southwest and backed with time from west-southwest to south-southwest in the top 30 m of the NEAR tower. The veering may possibly be caused by the increasing influence of katabatic flows from the terrain southwest and west of the crater with increasing height or may be an effect of surface friction (Ekman layer). The NEAR tower data are expected to be broadly representative of the katabatic layer upwind of the crater outside of the crater's influence.

Potential temperature (Fig. 3a) and wind profiles (Figs. 3b,d) above the rim were similar to profiles over the plain when displaced upward by the difference in elevations, indicating that the approaching air is lifted adiabatically over the rim. The colder potential temperatures near the ground on the NEAR tower are, however,

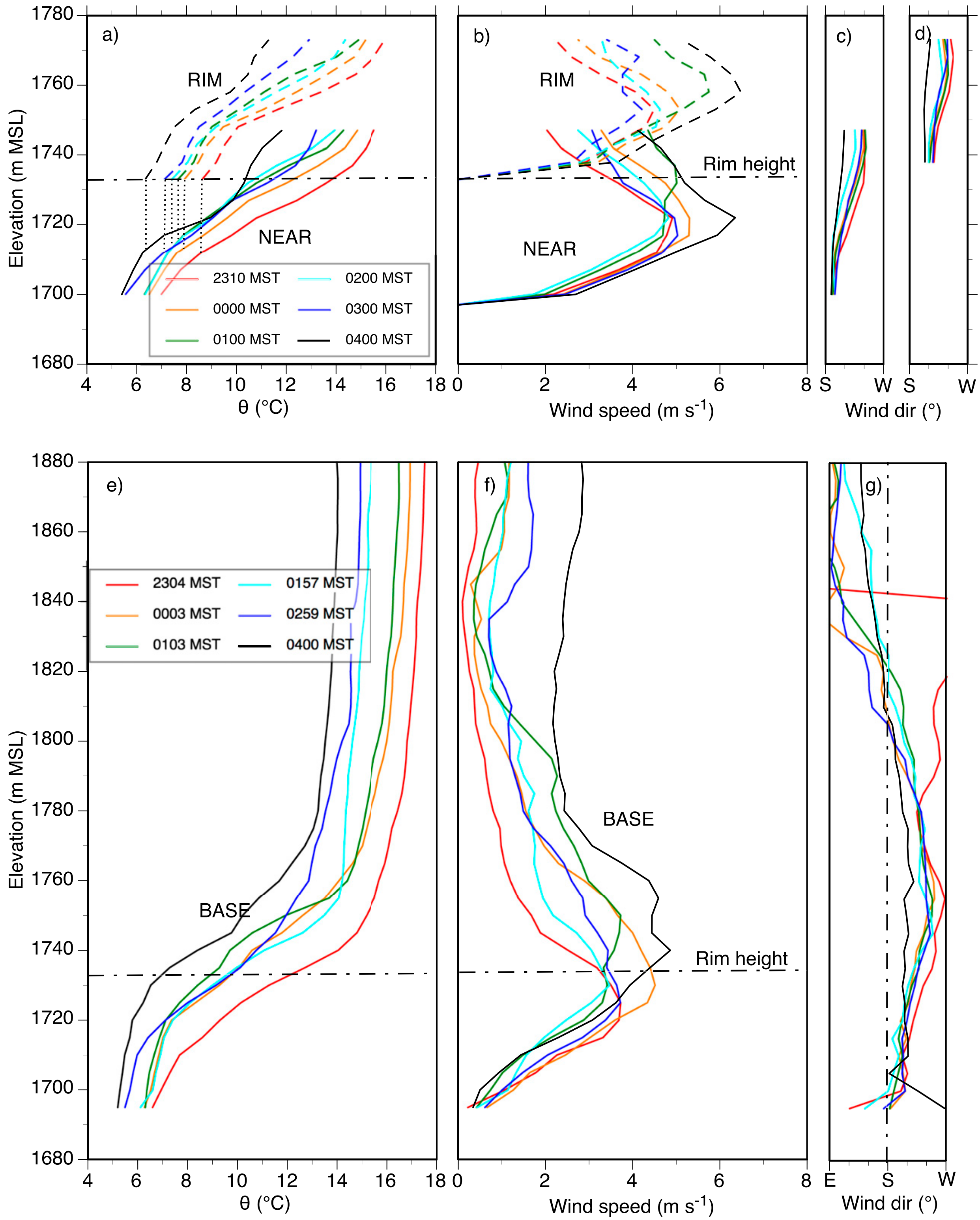

FIG. 3. (a) Potential temperature and (b) wind speed profiles on the NEAR and RIM towers for selected times (10-min mean). The first data points in the NEAR and RIM potential temperature profiles were at the 3- and 1.2-m (from a nearby HOBO) levels, respectively. The 0 m s^{-1} point has been added to the wind speed profiles at both tower bases. Vertical dotted lines in (a) translate potential temperatures downward from RIM to NEAR, illustrating the dividing streamline elevation and the cold air left behind in the lifting process. Also shown are wind direction profiles for (c) NEAR and (d) RIM. (e)–(g) Plots similar to those in (a)–(d), but for tethersonde TS-B; these are single rather than averaged soundings.

missing at the RIM tower. This low-level air, below a *dividing streamline* elevation (the elevation on the NEAR tower of the potential temperature at the base of the RIM tower; discussed in detail in section 4c), is carried around the crater rather than being lifted over the crater rim. A notable decrease in static stability of the air carried over the rim is present at the lowest layer of the RIM tower (Fig. 3a). An observed sensible heat flux divergence that increases with height in this shallow layer as it approaches the crater rim (a diabatic process) would contribute to this destabilization. Thus, our dividing streamline elevations calculated by assuming adiabatic flow may be somewhat too high. Vertical stretching of this layer as it approaches the crater above the dividing streamline (an adiabatic process) may also play a role in decreasing the static stability.

The TS-B tethersonde site on the plain was closer to the crater and at a slightly lower elevation than the NEAR tower. Individual soundings there (Figs. 3e–g) extended well above the NEAR and RIM towers. These deep soundings show that the NEAR tower was not quite high enough to encompass the full surface-based katabatic stable layer, which extended generally to 1745–1760 m MSL (Fig. 3e), as determined from the sudden change in stability at the top of the katabatic layer. Wind speeds (Fig. 3f) at corresponding elevations were weaker at this site than at either the NEAR or RIM tower, especially at the lowest levels where the flow was splitting around the crater. The katabatic flow extended to about 1840 m MSL (i.e., about 145 m above the plain). Wind direction profiles (Fig. 3g) were similar to those at NEAR and RIM.

b. *Spatial patterns of potential temperature and wind outside the crater*

The spatial variation of near-surface potential temperatures and winds from automatic weather stations and short towers as averaged over the 2300–0400 MST period is shown in Fig. 4. The main features on the plain upwind of the crater are the approaching southerly flow at NEAR, flow stagnation and coldest air upwind of the crater at SWP (see Fig. 1 for all the location types), splitting of the approaching flow around the southwest and southeast sides of the crater (WP and SEP), and near-surface potential temperature increasing as the crater rim is approached. Warmer air is found on the plain downwind of the crater, where the wind speed at NEP is reduced from that in the undisturbed flow upwind of the crater at NEAR. Atmospheric stability downwind of the crater (estimated from the temperature difference between the crater rim and the downwind plain at NEP) is much weaker than the upwind stability (based on the difference between the rim and the upwind plain), an indication that vertical mixing is occurring in the crater's wake. The processes leading to this mixing could not be determined from the limited data there.

Near-surface winds at the rim are much stronger than at sites on the upwind plain that are below the dividing streamline elevation. The wind directions on the upwind half of the crater rim are consistently from the approaching flow direction (i.e., from the south-southwest), with strongest winds on the west and northwest rim and with somewhat weaker winds on the south-southwest and southeast rims at RIM and SER. Because the amount of lifting above the dividing streamline required to surmount the rim (i.e., elevation difference between the dividing streamline at NEAR and the rim elevation) is similar at RIM, WR, and NWR (to be seen later in Fig. 6d with SSW′, WR, and NWR), loss of kinetic energy due to lifting cannot fully explain the speed reduction at RIM, which may be caused by the orientation of the saddle where the tower was located, as this was not oriented directly into the approach flow direction. On the downwind half of the crater rim, relatively weak warm outflows (i.e., relative to inflows over the upwind rim) exit the crater. These outflows are warm (Fig. 4) relative to inflows over the upwind rim (except for NR, which is located inside the crater several meters below the rim).

Figure 5 provides further evidence for the steadiness of the winds on the plain (Figs. 5a,b), at the rim (Figs. 5c,d), and inside the crater (Figs. 5e,f) between 2300 and 0400 MST. Winds at 5 m AGL on the RIM tower were typically $2.5 \pm 0.5\,\mathrm{m\,s^{-1}}$ during the steady-state period, with these winds backing about 30° over the period of interest (cf. Fig. 3d). Winds in the cold pool on the crater floor (Figs. 5e,f) were typically below $1\,\mathrm{m\,s^{-1}}$, but with a tendency to be from the south-southwest or north-northeast, parallel to the incoming flow direction. Winds at SSW2 and SSW4 will be discussed in section 5b. Average winds above the crater at the TS-B and TS-C sites (Figs. 5g,h) for the elevation interval between 1830 and 1850 m MSL (approximately 100 m above the rim) were generally below $2\,\mathrm{m\,s^{-1}}$ but increased gradually to reach $3.5\,\mathrm{m\,s^{-1}}$ between 0300 and 0400 MST. They maintained this speed until about 0500 MST and then fell to $2\,\mathrm{m\,s^{-1}}$ or less by 0600 MST. Wind directions aloft before the near-steady-state period were northerly. The veering of these winds to easterly or southeasterly initiated the near-steady-state period.

Winds were more variable at the ground-based sites before and after the steady-state period. The katabatic wind directions were attained at the plain and rim sites by about 2000 MST, with speeds then ramping up relatively quickly at the plains sites and more slowly at the

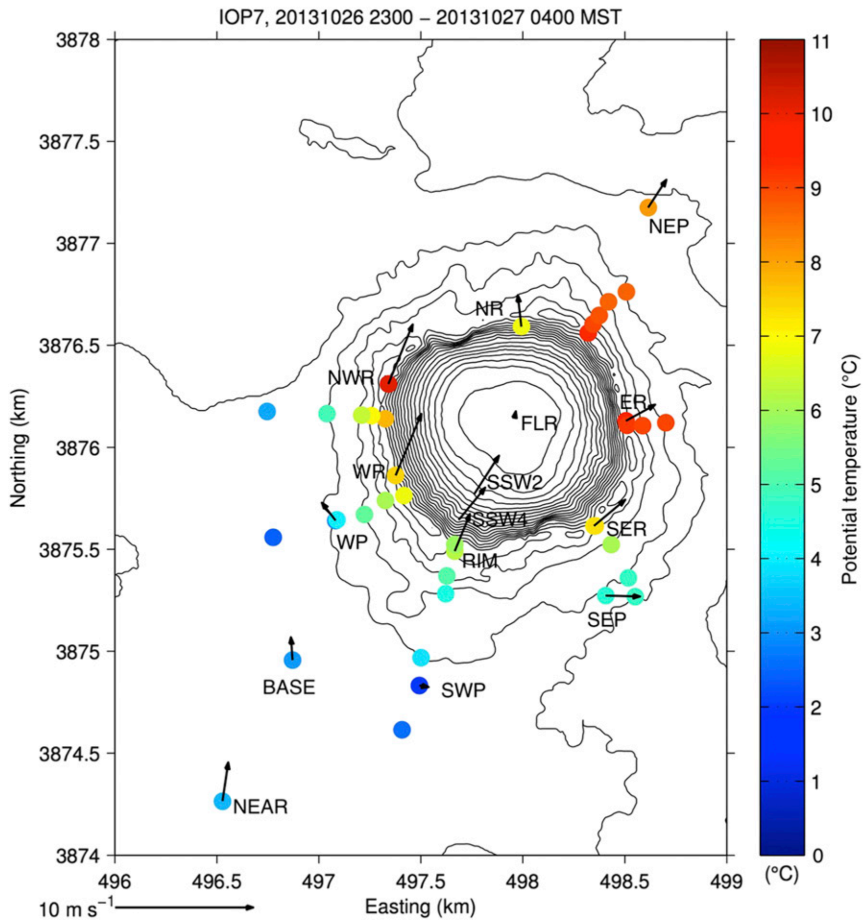

FIG. 4. Mean vector winds from 2300–0400 MST during IOP7. Wind measurements are at 2 m AGL, except at NEAR (3 m), RIM (5 m), SSW2 and SSW4 (3 m), and FLR and BASE (10 m). Temperature measurements (colored dots) are at 1.2 m AGL except at NEAR (3 m), RIM (5 m), FLR (2 m), and BASE (2 m).

rim sites to attain the speeds characteristic of the near-steady-state period. Wind directions were maintained after the steady-state period, but there was a short-term drop in wind speeds at the rim and basin sites between 0415 and 0500 MST.

c. *Dividing streamline elevations and the lifting of the stable layer over the rim*

The temporal variations of key meteorological variables on the plain and at the crater rim are shown in Fig. 6. Stability built up gradually on the NEAR tower beginning at 1830 MST, initiating a katabatic wind that increased in depth and first reached the top of the tower one hour later, as indicated by a wind shift into the west-southwest (Fig. 6a). The cold air intrusion over the crater rim began at about 1920 MST (Fig. 6b). Cold air surges were noted in the evening at some rim sites at 2050 and 2145 MST, but they were largely absent later in the night during the near-steady-state period, except for a surge at 0110 MST. There is a general nighttime cooling trend at all sites but at a given time potential temperatures vary around the rim, with the lowest potential temperatures at the upwind rim sites. The east rim had about the same potential temperature as the northeast rim while the northwest rim, on account of its higher elevation in the statically stable atmosphere, was warmer than the northeast rim. During the near-steady-state period the dividing streamline elevations on the plain upwind of the crater range from 1715 to 1735 m MSL (18–38 m AGL), with air coming over the upwind or SSW rim originating at the lowest of these elevations (Fig. 6c).

Lifting heights, the vertical distance that the approaching airflow must be lifted adiabatically from the NEAR tower to obtain the potential temperatures observed at the rim, are greatest at the SW rim where the topography is higher than at the SSW rim (Fig. 6d). The elevation difference between these two sites

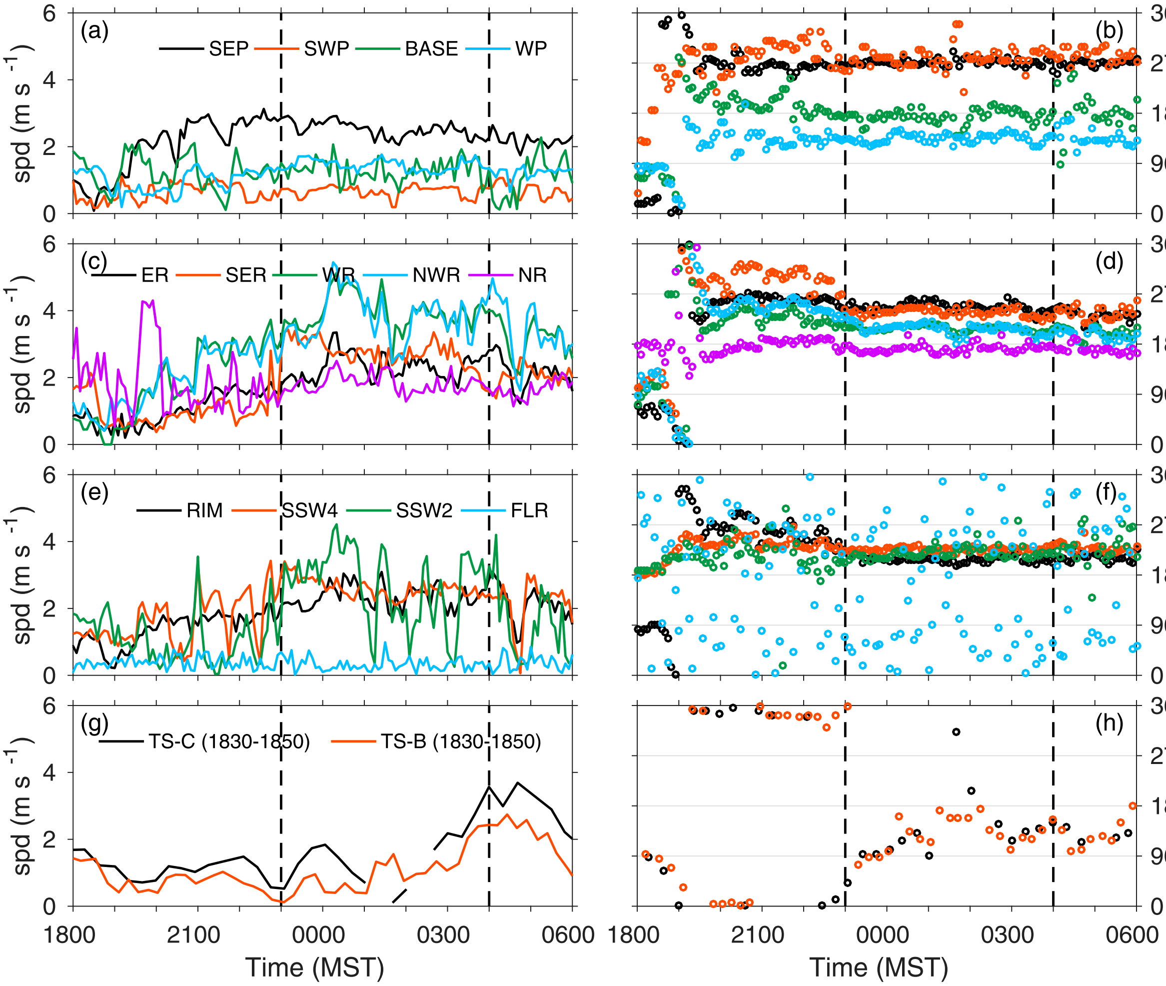

FIG. 5. Wind (a) speeds and (b) directions on the plain, wind (c) speeds and (d) directions on the rim, wind (e) speeds and (f) directions inside the crater, and tethersonde wind (g) speeds and (h) directions above the crater at TS-B and TS-C as averaged over the elevation interval from 1830 to 1850 m MSL. Dashed vertical lines indicate the beginning and end of the near-steady-state period.

exceeds the dividing streamline elevation differences. The greatest lifting and thus intrusion of coldest air occurs over the portion of the rim that is oriented into the approaching flow direction, with some variations caused by differing rim elevations (Fig. 2), with lower passes or gaps receiving relatively colder air.

The absolute angular distance of a measurement site on the rim from the direct upwind direction $|\Delta\phi|$, where $\Delta\phi$ is the difference between the bearing from the crater center to the given site minus the upwind direction at the jet maximum height on the NEAR tower, varies as the wind direction shifts in the approaching flow (Fig. 6e). In comparing Figs. 6b and 6e, it is seen that the coldest temperatures in IOP7 occur at the sites that are directly oriented into the upwind direction, with temperatures increasing with clockwise or counterclockwise angular distance around the rim $|\Delta\phi|$. This relationship is a general feature of katabatic flow over the circular crater rim as seen from an analysis using data from other suitable IOPs in which the effects of differing rim heights are removed by projecting the temperatures to a common reference elevation (Fig. 7). The potential temperature deviation (K) from the coldest upwind site depends on the cosine of angular distance following the formula $\Delta\theta = 4.82 + 4.39\cos(\Delta\phi + 173°)$. Air coming over the most directly upwind portion of the rim is lifted from elevations closer to the surface of the surrounding plain where temperatures are lower. Air is lifted from progressively higher, warmer elevations as one progresses clockwise or counterclockwise around the crater rim. In other words, the dividing streamline elevation is lowest directly upwind of the crater and rises to the left and right on a vertical plane oriented perpendicular to the oncoming flow direction.

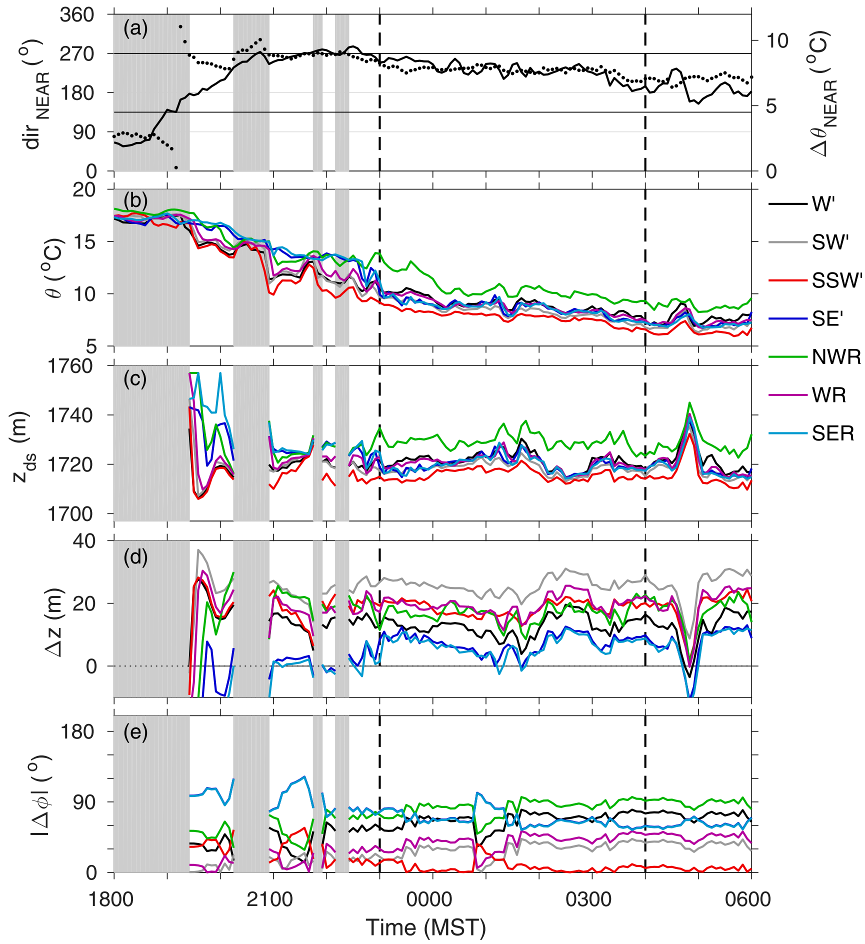

FIG. 6. Temporal variations of the (a) 50-m AGL wind direction (dotted) and the 50 m − 3 m AGL potential temperature difference (solid) on the NEAR tower, (b) potential temperatures at the rim sites, (c) dividing streamline elevations, (d) adiabatic lifting required above the dividing streamline to reach the rim sites, and (e) deviation of the rim site bearing from the approaching wind bearing (wind direction minus 180°) at the height of the jet maximum on the NEAR tower. Gray shading indicates times when the wind direction at 50 m AGL at NEAR was not directed down the mesoscale slope (outside 135°–270°). Dashed vertical lines indicate the beginning and end of the near-steady-state period.

5. Atmospheric structure inside the crater

a. *Potential temperature and wind speed profiles*

The lifting of the katabatic layer over the upwind rim provides a continuous source of cold air that flows down the upwind sidewall into the basin. In this section the potential temperature and wind fields are investigated to determine the atmospheric response inside the crater.

Mean profiles of potential temperature, wind speed, and wind direction from a line of sites on a vertical cross section oriented approximately along the wind and crossing through the crater during the near-steady-state period are shown in Fig. 8, including tethersonde profiles at the TS-SW and TS-C sites and pseudovertical profiles from the SW, SSW, and NE HOBO lines obtained by plotting potential temperatures as a function of the HOBO elevations (Fig. 8a). The pseudovertical profiles are thus modified along-slope profiles rather than vertical free atmosphere profiles. Also shown in the figure, for comparison, are profiles from outside the crater at the NEAR and RIM towers and at the TS-B site. The TS-SW profile and, to a lesser extent, the TS-C profile, as we will see later in the wind speed profiles, are affected by the intrusions on the upwind side of the crater. The NE profile, on the opposite sidewall from the intrusions, is most representative of an undisturbed basic state profile inside the crater and the NE and SSW profiles are both on a slope where some of the same physical processes are

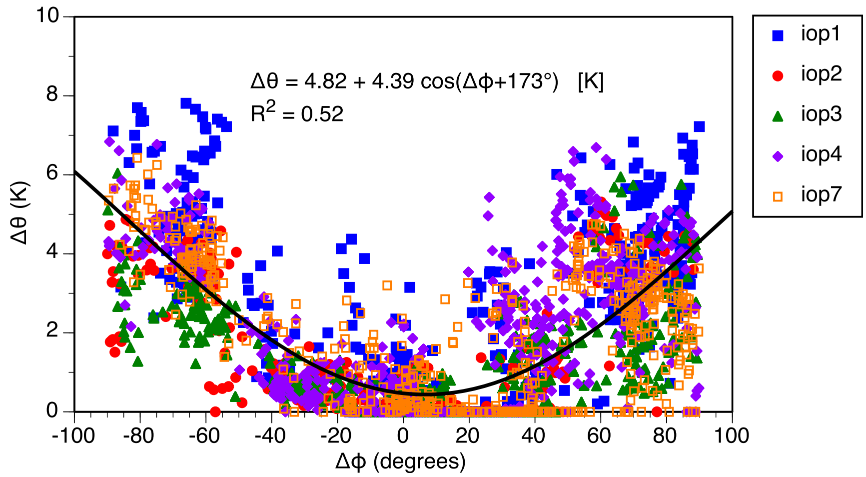

FIG. 7. Potential temperature difference $\Delta\theta$ around the crater rim at a reference elevation of 1745 m MSL vs the angular differences $\Delta\phi$ between the wind directions at the jet maximum height on the NEAR tower and the bearings to the individual rim sites for selected IOPs (see legend). The analysis uses 5-min data for nighttime periods (1800–0600 MST) when both a statically stable layer ($\theta_{50m} > \theta_{3m}$) and a downslope flow ($135° < \phi_{50m} < 270°$) at the top of the 50-m-high NEAR tower were present. Projections to the 1745-m level use the RIM tower θ profile, θ at the selected rim site, and the elevation difference d between the selected site and 1745 m. The projected temperature is the temperature at distance d above the elevation in the RIM θ profile where θ matched that of the rim site. The previously noted adiabatic lifting of air over the rim suggests this approach, as the RIM profile can be considered fixed and simply adjusted vertically as it passes over other upwind rim sites.

operating (radiative cooling to similar sky view factors and nearness to the underlying surface). The NE profile has a similar structure to the central TS-C profile but is a fraction of a degree colder. In agreement with METCRAX observations (Whiteman et al. 2010), the main features of the undisturbed (NE) potential temperature profiles within the crater are a stably stratified layer with a 5–10-K potential temperature deficit of about 30–40-m depth on the crater floor (the *cold pool*) surmounted by a near-isothermal layer comprising the upper 75%–80% of the crater atmosphere. A potential temperature jump occurs at and just above rim level on all crater soundings, indicating that the crater atmosphere cools significantly during the night relative to the residual layer above the crater.

The katabatic stable layer on the plain (TS-B) is lifted over the crater rim (RIM). The lower part of the stable layer is negatively buoyant with respect to the air in the crater and descends the southwest sidewall, while the upper nonnegatively buoyant part is carried quasi-horizontally over the crater. This flow bifurcation produces a cavity or wake in the lee of the rim with constant potential temperature in the TS-SW profile (Fig. 8a). The descent of negatively buoyant air into the crater causes the coldest portion of the stable layer coming over the rim to be missing in the capping inversion of the TS-SW, TS-C, and NE profiles. Potential temperatures on the upwind rims (SSW′ and SW′) are 2–3 K colder than the NE rim, as relatively cold air flows over the upwind rim. The pseudovertical profiles on the upwind inner sidewall of the crater (SSW and SW) have a superadiabatic stability that is thought to be caused by turbulent mixing as the cold air intrusion layer descends the sidewall. The superadiabatic stability is a persistent feature that was also noted in METCRAX (Whiteman et al. 2010). The base of the superadiabatic layer where it typically intersects with the background NE profile represents a *neutral buoyancy elevation* (NBE), where the base of the cold air intrusion reaches its level of buoyancy equilibrium.

The jet-like katabatic speed profile seen in the NEAR and TS-B profiles (Fig. 8b) is lifted over the crater rim (RIM). A weak jetlike profile occurs in the 1740–1800-m MSL layer above the rim at TS-SW and TS-C, indicating the quasi-horizontal overflow of the upper portion of the stable layer over the crater. Wind speeds are weak inside the crater except for a speed maximum in a 50-m-deep surface-based wind layer at TS-SW just above the top of the cold pool as a result of inflow of air from the southwest sidewall. This layer, while present, is less apparent at TS-C. Synoptic flows above the crater on this night are quiescent, as indicated by the wind speed minimum at 1825 m MSL in the TS-B, TS-SW, and TS-C profiles.

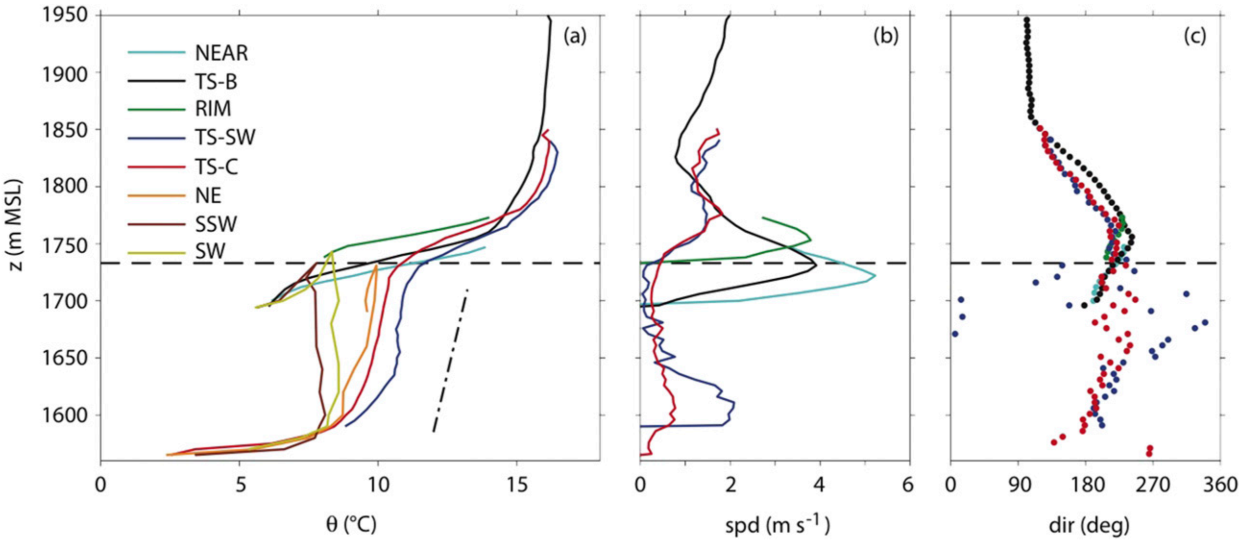

FIG. 8. Five-hour-mean (2300–0400 MST) (a) θ, (b) wind speed, and (c) wind direction profiles. Winds at TS-SW and TS-C are excluded for elevations that were attained by fewer than 50% of the soundings. Also shown are observations from the NE, SSW, and SW HOBO lines, including potential temperatures on the adjacent plain. The rim level is indicated by the horizontal dashed line. An isothermal temperature gradient is indicated by the slope of the dot–dashed line in (a).

Wind directions (Fig. 8c) inside the crater are from the SSW, the katabatic flow direction on the plain outside the crater, except for variable directions in the TS-SW profile in a layer in the upper half of the crater where the mean stability (Fig. 8a) is near-neutral. A lesser wind direction variability is also seen in this layer at TS-C.

b. Variability

Hourly profiles (Fig. 9) illustrate the potential temperature variability inside the crater during the steady-state period and the calculated NBEs. The NBEs are the highest elevations where the upwind profiles have the same potential temperature as the background (NE) profiles. These generally occur at the base of the superadiabatic layers. In occasional cases where the profiles do not cross, the base of the superadiabatic layer can be used as an alternate estimate of the NBE. Crossings of the profiles indicate that the cold-air intrusion *overshoots* its level of buoyancy equilibrium. The potential temperature structure and the relative potential temperature profiles among the sites vary little with time, except at the crater floor when the cold pool is occasionally disturbed by the cold air intrusion. The variation with time of the NBEs is primarily a function of the differing negative buoyancies of the air overflowing the rim, with lower NBEs on lines where the negative buoyancy is greater.

Temporal variations of key variables inside the crater are shown in Fig. 10, including potential temperatures at the basin floor surface (S) and at the upwind (U_i, where i = 1–3 for the SSW′, SW′, and W′ sites, respectively) and downwind (NE′) rim sites, and differences ($\Delta\theta_i$) between the NE′ and S sites (NE′ − S), the NE′ and upwind sites (NE′ − U_i'), and the NBEs and crater floor surface (NBE$_i$ − S). Also shown are NBEs and potential temperature gradients γ_i between the rim sites and the NBEs (U_i' − NBE$_i$). Following Mahrt and Heald (2015), various combinations of these variables aid in identifying key physical characteristics of the atmospheric structure and physical processes. For example, $\theta_{\mathrm{NE}'} - \theta_{\mathrm{Ui}'}$ is proportional to the negative buoyancy of the inflows. Also, $\theta_{\mathrm{NE}'} - \theta_S$ is a measure of bulk atmospheric stability and NE′ − S is the sum of the stability increments above ($\theta_{\mathrm{NE}'} - \theta_{\mathrm{NBEi}}$) and below ($\theta_{\mathrm{NBEi}} - \theta_S$) the NBE.

Potential temperatures at the rim sites decreased rather steadily through the period, with significant differences among the rim sites and between the sites and the northeast line (Fig. 10a). The bulk stability inside the crater $\theta_{\mathrm{NE}'} - \theta_S$ varied over the range from 11 to 6 K, with most of this variation ($\theta_{\mathrm{NBEi}} - \theta_S$) occurring below the NBE (Fig. 10b) and driven by potential temperature changes at the crater floor. NBEs (Fig. 10c) varied on the three upwind HOBO lines and were lowest on the SSW line. Because wind directions were more westerly in the early part of the period and then backed over time, NBEs on the SW and SSW lines were initially low but then increased with time. NBEs on the W line were found about halfway down into the crater basin. The average pseudovertical temperature gradient from the rim to the neutral buoyancy elevation was variable

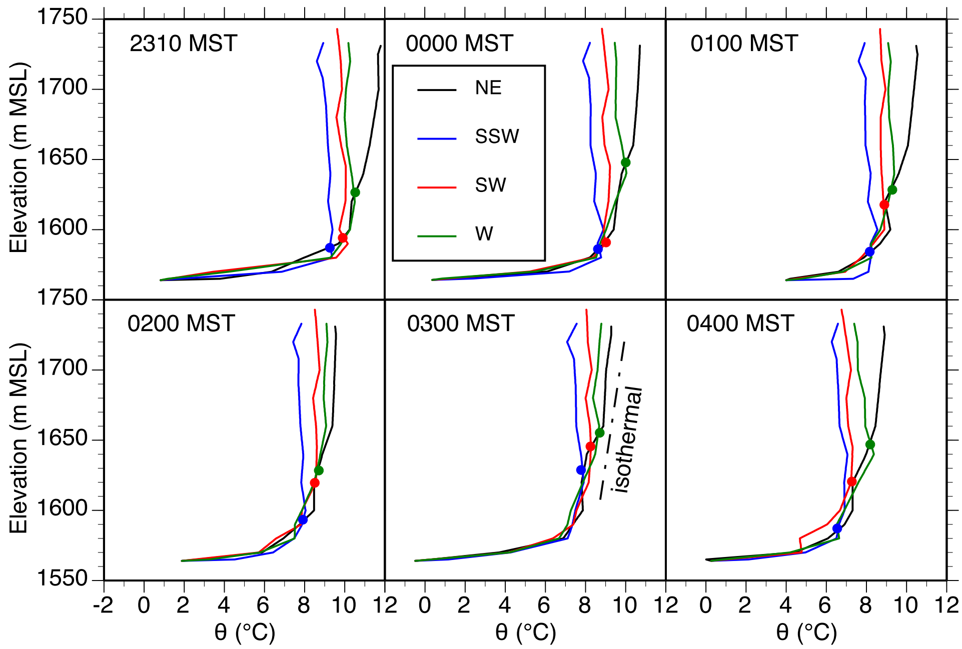

FIG. 9. Five-minute mean pseudovertical θ profiles for four HOBO lines at selected times during the near-steady-state period. Colored dots indicate the points where the colored lines cross the black line (i.e., the neutral buoyancy elevations). An isothermal temperature gradient ($dT/dz = 0°C\,m^{-1}$) is indicated by the dash–dotted line in the 0300 MST panel.

but generally slightly superadiabatic (i.e., negative; Fig. 10d).

c. *Detrainment, buoyancy, and layer-based neutral buoyancy elevations*

Cold air intrusions come over the rim and run down the upwind inner sidewall. This inflow can be visualized as a column of cold air. The lowest portion of the stably stratified column with potential temperatures colder than the downwind rim will have the negative buoyancy necessary to descend into the crater. As the column descends the sidewall the column's upper levels will reach their NBEs first and will detrain into the ambient atmosphere. This *buoyancy sorting* has been observed in previous laboratory simulations (Baines 1995) and is a feature of cumulus convection models (Emanuel and Raymond 1993). As the column descends the sidewall its negative buoyancy will decrease due to 1) the decreasing potential temperatures of the ambient atmosphere as the floor is approached and 2) the increasing potential temperatures at the column's base as elevation decreases because of turbulent mixing at the base of the descending cold airstream, leading to superadiabatic pseudovertical potential temperature gradients ($\gamma_i < 0$) between the elevations of the upwind rims and their corresponding neutral buoyancy elevations. Such superadiabatic profiles are not found in free air soundings over the basin center or in the proxy pseudovertical profiles on the NE sidewall. Pseudovertical superadiabatic profiles are quite atypical in basins and valleys during nighttime, as sidewall temperatures usually reflect the strong static stability of free air profiles over the basin or valley center. One must be careful not to attribute the same meaning to these along-slope profiles as one would to free air profiles. They do not, for example, mean that vertical convection will occur along or above the sidewall. However, such gradients may be a useful diagnostic indicator of cold air intrusions.

The NBEs, discussed in sections 5a and 5b, are parcel-based. The cold air intrusion coming down the sidewalls, however, is a layer, and the elevation where the mean potential temperature of the intruding layer matches the potential temperature of the undisturbed crater environment is an alternative layer-based neutral buoyancy elevation (LNBE). The LNBE can be estimated for each line with the approach diagramed in Fig. 11 using data from the RIM tower and the NE and upwind HOBO lines. This approach assumes that Δ does not change with distance down the sidewall, thus ignoring the minor superadiabatic warming at the surface. The LNBEs are higher than the parcel-based NBEs in Figs. 9 and 10. The result for the SSW line is shown as the black line in Fig. 12. LNBEs were lower and much more variable on the SSW line than on the other HOBO lines (not

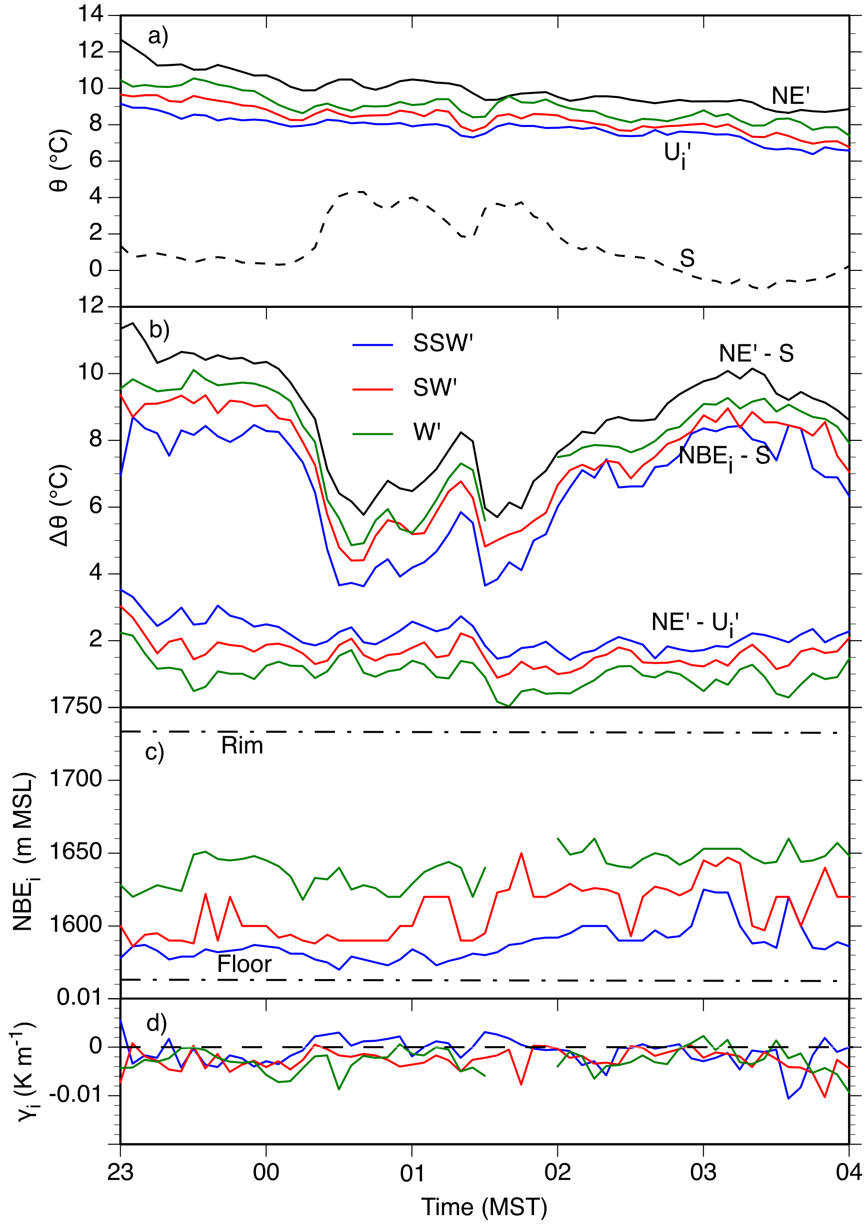

FIG. 10. Variation with time of (a) potential temperatures at the downwind (NE′) and upwind (U_i') rim sites (i = 1–3 for SSW′, SW′, and W′, respectively) and the basin floor (S); (b) θ differences between the downwind rim and the floor (NE′ − S), between the neutral buoyancy elevation and the floor (NBE_i − S), and between the downwind and upwind rims (NE′ − U_i'), again using the i index for the upwind sites; (c) neutral buoyancy elevations (NBE_i); and (d) θ gradients γ_i between the neutral buoyancy elevations (NBE_i) and the upwind rim elevations (U_i').

shown). The variability is caused by temporal variations in inflow characteristics at the rim (negative buoyancy and cold air depth) that propagate down the sidewalls.

d. *Wind speed oscillations at SSW2 and SSW4*

Wind speed oscillations at SSW4 and SSW2 (Fig. 12) are closely related to the LNBEs, which were sometimes above SSW4, and at other times between the two sites or below SSW2. At SSW4, speeds accelerate (decelerate) when the LNBE is below (above) this site and decelerate when the LNBE recedes up the sidewall, as seen in multiple events during the 1800–2300 and 0400–0600 MST periods. During the intervening 2300–0400 MST period, the cold air penetrates to elevations between

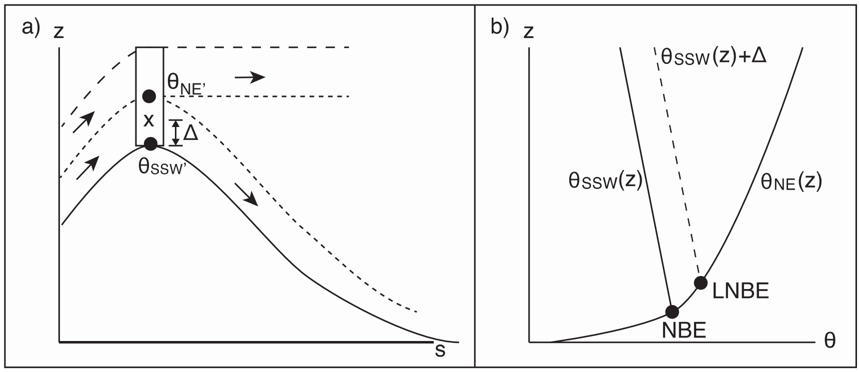

FIG. 11. LNBE definition, as illustrated for the SSW HOBO line. (a) Along-wind (s–z) terrain cross section (solid line) and the statically stable katabatic layer column carried over the rim (dashed and dotted lines are isentropes). (b) SSW and NE pseudovertical potential temperature profiles. The negatively buoyant layer is the lower portion of the statically stable layer coming over the rim having potential temperatures below $\theta_{\mathrm{NE}'}$. The 5-min-mean potential temperature difference Δ between the rim and the mean potential temperature (x) of the negatively buoyant layer in (a) is, in (b), added to the SSW pseudovertical potential temperature profile. The elevation of the crossing of the modified potential temperature profile with the NE profile is the LNBE. For lines other than the SSW line, the mean potential temperature is computed from the RIM tower profile for the layer between θ_i' and $\theta_{\mathrm{NE}'}$; Δ is then the difference between this mean potential temperature and θ_i'.

SSW4 and SSW2, producing relatively steady wind speeds at SSW4 with only small fluctuations caused by changes in the negative buoyancy of the inflow. The SSW2 site, in contrast, is generally submerged in the cold pool on the crater floor, with LNBEs above the site. Wind speeds are low when the site is submerged, but accelerate quickly when the cold-air intrusion reaches elevations close to or below SSW2. When the cold air inflow reached SSW2 the wind speeds were higher than at SSW4, providing evidence that the intrusion accelerates as it descends the sidewall. There are times when accelerations occur at SSW2 when the calculated LNBEs are above SSW2 (e.g., at 0230 MST). In these events the computed layer-based elevations may be too high or overshooting may play a role. An estimate of the penetration elevation caused by overshooting is shown by the green line in Fig. 12, determined from the steady-state along-slope integrated momentum equation

$$\frac{u_p^2}{2} = g\int_{s_p}^{s_0} \frac{\theta'}{\theta_0}\sin\alpha\, ds$$

by finding the downslope distance s_0 where the along-slope wind speed at the neutral buoyancy elevation (u_p) decreases to zero, taking account of the variation with downslope distance of the slope angle α, the potential temperature θ_0, and the potential temperature difference θ' between the SSW and NE HOBO lines. For this calculation, the wind measured at SSW4 at downslope distance s_p was assumed representative of u_p. Setting u_p to the jet maximum speed above SSW4 would further decrease the penetration elevations, while drag forces, ignored in the formulation, would increase the penetration elevations. The results (Fig. 12) suggest that the negative buoyancy of the cold-air inflow layer and the loss of its momentum due to overshooting could explain the penetration of the cold air into the crater and the wind speed observations on the SSW slope.

e. *Lidar observations of the wind field*

Doppler wind lidars were deployed on the north rim and the crater floor to make continuous range–height indicator (RHI) scans in a vertical plane oriented roughly along the incoming katabatic wind direction at 195° azimuth (Fig. 1). Doppler wind lidars measure radial velocities (i.e., the along-beam component of the wind field) and, by combining radial velocities from the two lidars, the two-dimensional flow field on a vertical cross section through the crater is obtained using a dual-Doppler retrieval approach documented by Cherukuru et al. (2015).

Dual-Doppler retrievals average all available scans in the vertical plane over a 2.5-min interval; the number of scans per retrieval can vary. Single Doppler retrievals were made over a 180° elevation range, taking 67 s to complete. An animation of 5-min-mean dual-Doppler retrievals and an accompanying caption can be found as a compressed file package in the online supplemental material. In this section, we present selected 5-min-mean wind retrievals for 2335–2340 MST (Fig. 13a) and 0220–0225 MST (Fig. 13b), as well as the average for the

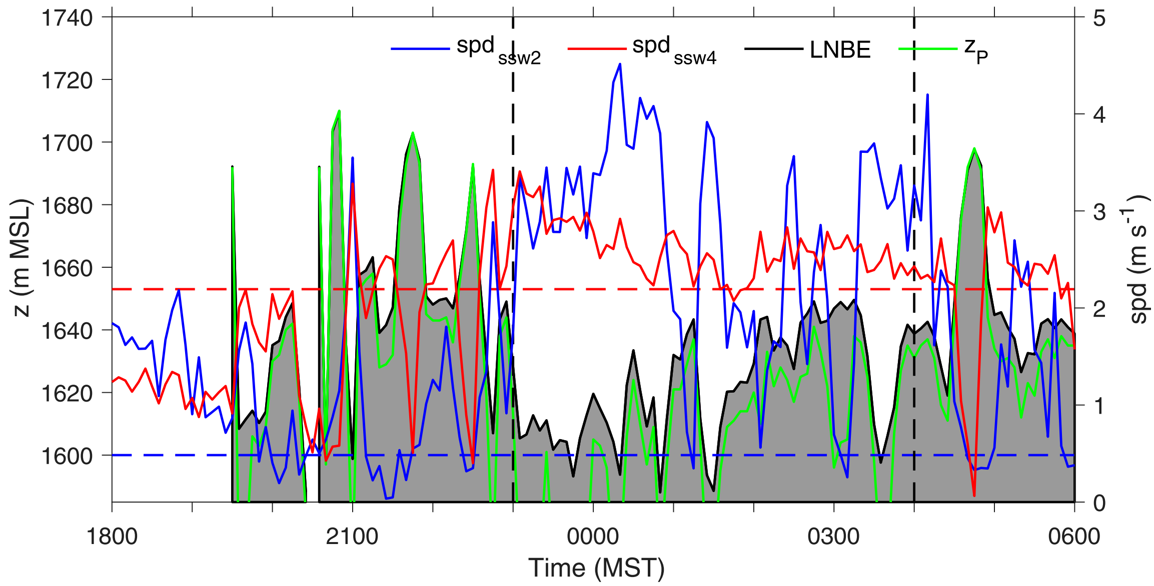

FIG. 12. Time–height cross section of LNBE and penetration elevation (z_p; green) on the SSW sidewall and their relationship to wind speeds at SSW4 (red) and SSW2 (blue). Dashed red and blue lines indicate the elevations of SSW4 and SSW2, respectively. Dashed vertical lines indicate the beginning and end of the near-steady-state period.

entire 2300–0400 MST period (Fig. 13c). In all three examples, air coming over the rim bifurcates with the upper current flowing over the crater above rim level (see also Fig. 8b) and the lower current of cold air descending into the crater along the sidewall. A wave is present in the lee of the upwind rim in the upper current in all examples, although the wave at 2335–2340 MST is much smaller in amplitude and wavelength than in the other images. A variable size wake or ‘‘cavity’’ containing weak winds (Figs. 13a–c) and neutral stability (Fig. 8) forms in the lee of the rim and extends downward into the basin. Winds in this cavity often have the appearance of a clockwise rotating horizontal-axis eddy, but the circulation is most often not closed at its lower extremity.

The lower cold current is best seen in radial velocity retrievals from the floor lidar RHI scans (Figs. 14a–c), as the lowest elevation angle beams are nearly parallel to the underlying sidewall so that radial velocities are good representations there of the along-slope speeds. However, at higher angles above the slope and above the upper sidewall the radial velocities are not representative of the along-slope intrusion. A strong isotach gradient delineates the top of the cold-air intrusion and a weak upslope countercurrent is often present above this inflow layer. Speeds in the intrusion are variable, but typically several meters per second. Highest speeds on the lower slope occur just upslope of SSW2. An along-slope deceleration just downslope of this maximum is frequently associated with a zone of rising motions above the slope, as seen in Fig. 13b. This zone is typically in the vicinity of or upslope of TS-SW. The upward motions are stronger at 0220–0225 than at 2335–2340 MST (cf. Figs. 13a,b). Such rising motions are sometimes absent in other images when downslope flows are weak (not shown), although they might be present but too shallow to be seen in the lidar retrievals. Downwind of the deceleration, the current tends to lift off (i.e., extrude from) the slope at an elevation above the NBE and the cold pool (Fig. 13b) to flow quasi-horizontally into the ambient isothermal layer above the cold pool. The rising motions associated with along-slope speed convergence at elevations where the layer reaches and overshoots its LNBE may be indicative of an atmospheric-analog *hydraulic jump*. This jump, while present in Fig. 13b, is de-emphasized in the mean flow field of Fig. 13c because of its intermittent nature and its excursions up and down the slope. Lidar evidence for a hydraulic jump is also supported by potential temperature data, as a rapid ascent of isentropes occurs on the crater cross section between TS-SW and TS-C. For example, the potential temperature at the base of the elevated neutral layer or cavity at ~1650 m at TS-SW is found at 1740 m in the TS-C profile (Fig. 8). The horizontal separation distance between these two sites is 320 m.

The varying wind speeds and directions in the two-dimensional wind retrievals (Figs. 13a–d) indicate a significant three dimensionality in the actual flow field. Bifurcations (dual-lidar retrievals) and downslope flows (single lidar retrievals) are present in all retrievals in the

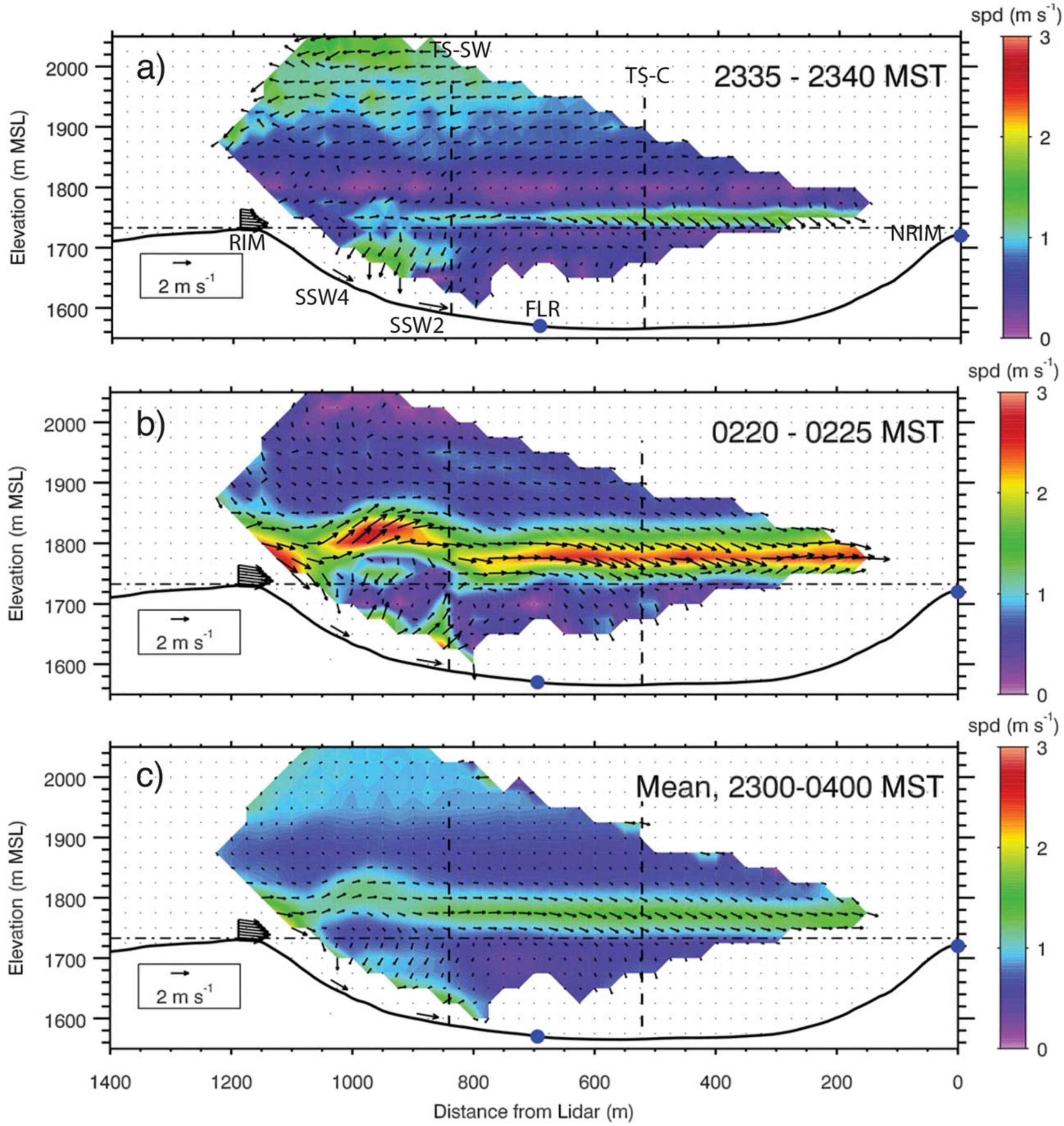

FIG. 13. Dual-Doppler lidar wind retrievals in a vertical (u–w) plane (green line in Fig. 1). Winds (vectors) and speeds (colors) at (a) 2335–2340 and (b) 0220–0225 MST, and (c) averaged over 2300–0400 MST. Measurement sites are indicated in (a). Blue circles indicate lidar locations. The x-axis origin is the NRIM lidar.

2300–0400 MST period, while wave amplitudes and wavelength, the cavity size, the maximum wind speed and depth of the downslope flow, and the position of the hydraulic jump on the slope are all variable (again, see the animation in the supplemental information). We cannot say unequivocally whether the cold air intrusion is deepening or thinning as it descends into the crater basin because radial wind retrievals on the upper slope include horizontal overflow and wave contributions, and dual lidar retrievals cannot get close to the slope because the NRIM lidar views the slope at a high incidence angle and the first range gate intersecting the slope must be discarded. Entrainment and orographically induced flow convergence as the crater floor

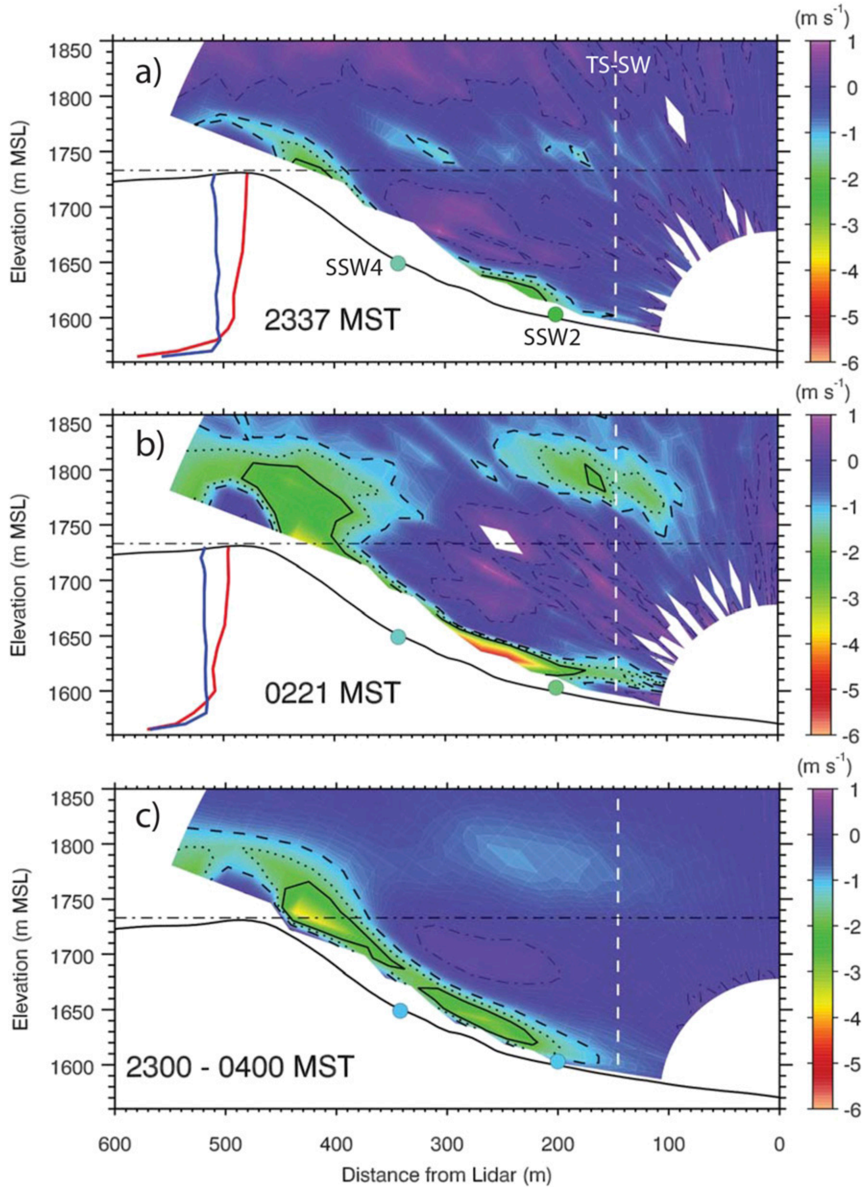

FIG. 14. Lidar radial wind speed (see color legend) retrievals from RHI scans at the FLR site at (a) 2337 and (b) 0221 MST, and (c) as averaged over 2300–4000 MST. The x-axis origin is the FLR lidar, and negative speeds are toward the lidar. Solid, dotted, dashed, and dot–dashed contours are 2, 1.5, 1, and 0 m s^{-1} isotachs. SSW2 and SSW4 measurement sites are identified in (a), and colors within circles indicate downslope wind components at 3 m AGL at these sites. Contemporaneous pseudovertical θ profiles from the SSW (blue) and NE (red) HOBO lines are shown in (a) and (b).

is approached would cause the intrusion to deepen, while detrainment at its top during its descent would cause it to thin. The single lidar retrievals show that the cold-air intrusion deepens to ~60 m and strengthens (reaching ~5 m s^{-1}) during the 0006–0050, 0116–0126, and 0340–0400 MST intervals (not shown). Stronger and deeper vertical motions occur above the lower south-southwest sidewall during these times, which coincide with temporarily stronger inflows over the rim and at SSW2 (Fig. 5e) and potential temperature rises (Fig. 10a) on the crater floor that may be produced by advection of turbulence produced in the hydraulic jump or by vertical mixing caused by shear associated with the quasi-horizontal extrusion.

6. Froude number assessment

A key dynamical characteristic of an idealized two-layer atmospheric flow is its nondimensional Froude number $F = (\pi/2)(U/HN)$ (Rotunno and Lehner 2016), where U is flow speed (assumed constant), H is lower-layer depth characterized by Brunt Väisälä frequency $N = [(g/\theta)(\partial\theta/\partial z)]^{1/2}$, and the upper, infinite layer has $N = 0$. Here, g is gravitational acceleration, θ is potential temperature, and z is height. A supercritical flow ($F > 1$) implies that the speed of upstream propagation of gravity waves is slower than the approaching flow, so that information on disturbances to the flow does not propagate upstream. Computations of F for a continuously stratified atmosphere with wind speeds changing with height are problematic and our calculations using either flow depth (whether above ground or above the dividing streamline) or inversion depth for H, typical upstream values of mean and maximum wind speeds for U and mean values of N produce F values ranging between subcritical and supercritical (0.5–2.8). Idealized model simulations (Lehner et al. 2016a) for a basin with no rim suggest that the flow upstream of the basin would be supercritical to support the flow pattern observed in the lee of the crater rim. An alternative Scorer parameter method using Benjamin's (1962) criticality test as evaluated numerically with observations [see the Lehner et al. (2016a) appendix for this approach] suggests that the flow approaching the crater is subcritical. Thus, we cannot make a clear assessment of the criticality of the flow upstream of the crater. However, using RIM tower profiles from Fig. 8, the negatively buoyant portion of the flow over the crater rim is supercritical (F between 1.8 and 3.5 with $H \sim 25\,\mathrm{m}$, $N \sim 0.071\,\mathrm{s}^{-1}$, and mean and peak speeds $U \sim 2$ and $4\,\mathrm{m\,s}^{-1}$). From Rotunno and Lehner (2016), the upstream supercritical flow can be expected to remain supercritical as the flow descends the slope, while the Froude number of the weak flow over the valley center is clearly subcritical. The supercritical to subcritical transition between the lower slope and the valley center further supports the hydraulic jump hypothesis.

7. Conceptual model

A conceptual model of the katabatically driven cold air intrusions into the Meteor Crater basin during the clear, undisturbed steady-state period of IOP7, as supported by the analyses in sections 4–6, is presented in Fig. 15.

A continuous jetlike katabatic flow approaches the crater from the southwest. The jet maximum is embedded in a ground-based statically stable layer that forms over the tilted plain. Vertical momentum transport causes the katabatic flow to extend above the stable layer into the slightly stable, quiescent residual layer. At elevations on the plain below a *dividing streamline* the katabatic flow slows upwind of the crater and *splits* around the crater. Above the three-dimensional dividing streamline surface the air is lifted adiabatically over the rim. Dividing streamline elevations increase and vertical lifting decreases with angular distance away from the upwind rim, producing warmer inflows and smaller katabatic overflow depths.

The negatively buoyant lower portion of the lifted stable layer with $\theta < \theta_{NE'}$ turns down the sidewall and intrudes into the crater, descending the inner sidewall. The nonnegatively buoyant upper portion of the lifted stable layer with $\theta > \theta_{NE'}$ is advected quasi-horizontally over the basin. A low-amplitude *wave* often forms downwind of the rim in this overflow. The *bifurcation* of the nonnegatively and negatively buoyant currents occurs above the crater rim, creating a neutral stability *cavity* or wake of low wind speed in the immediate lee of the rim that has the same (bifurcated) isentrope above and below the cavity. This cavity is similar to that noted by Winters and Armi (2014) in simulated flows over a ridge. The negatively buoyant cold air intrusion accelerates down the slope. Its negative buoyancy, determined at any height by its layer potential temperature deficit relative to that of the undisturbed air at that height within the crater, decreases with downslope distance. The undisturbed air within the crater consists of a shallow but strongly stable *cold pool* on the crater floor, with an *isothermal layer* above, surmounted by a potential temperature jump to connect it to the warmer residual layer above the crater. Turbulent mixing within the cold-air intrusion produces a near-surface, along-slope, superadiabatic temperature gradient. Detrainment from the top of the intrusion is hypothesized to occur as the flow descends the sidewall. The deepest penetration of the cold-air intrusion occurs on the upwind inner sidewall where the inflow layer is colder and deeper; *penetration depths* decrease with angular distance away from the upwind direction. The intrusion, as it penetrates deeper into the crater, *overshoots* its *layer-based neutral buoyancy elevation* and initiates a *hydraulic jump*, with much of the flow directed upward and the remaining flow extruding quasi-horizontally into the ambient crater atmosphere. A weak classical downslope flow may separately occur on the slope below and on all crater slopes unaffected by the cold air intrusion. The turbulent hydraulic jump, which transitions the flow from a shallow supercritical high-speed flow to a deeper, lower speed subcritical flow, moves intermittently up and down the slope. A continuous *outflow*, enhanced somewhat through passes and gaps, occurs over the downwind

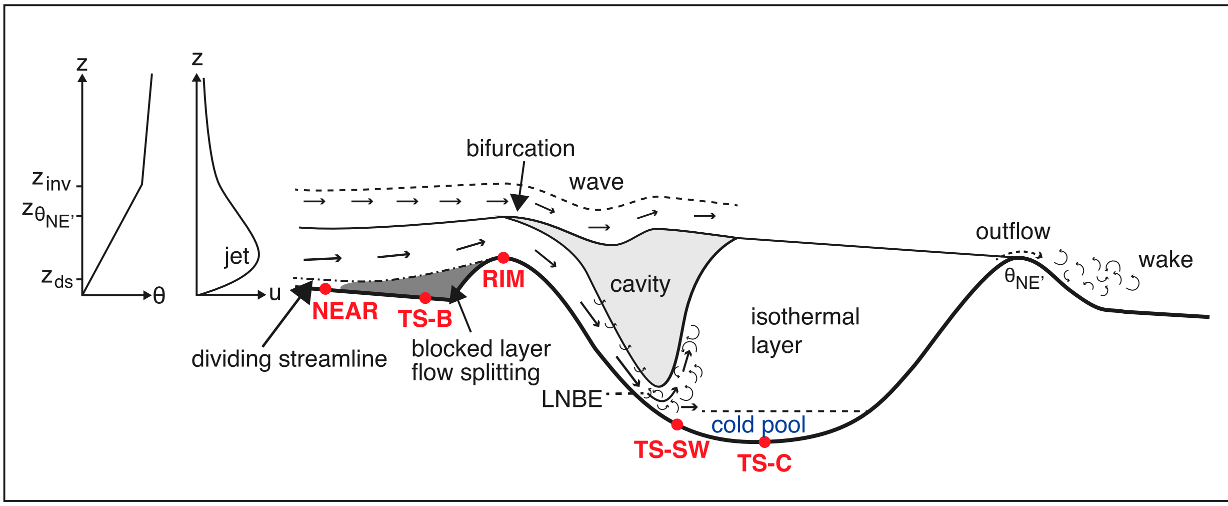

FIG. 15. Conceptual model on an along-wind cross section (not to scale) showing the interactions of the katabatic flow on the plain with a rim-enclosed basin. Relative locations for named vertical profiling sites are indicated by red circles. Here z_{INV} is the stable layer height, $z_{\theta\mathrm{NE}'}$ is the height on the upstream plain of the potential temperature $\theta_{\mathrm{NE}'}$ at the downwind rim, and z_{ds} is the height of the dividing streamline on the plain far upwind of the crater. LNBE is the layer-based neutral buoyancy elevation. The relatively warm cavity contains a near-neutral (well mixed) atmosphere.

half of the crater's rim to balance the cold air inflow in the upwind half. A well-mixed *wake* forms in the lee of the crater.

8. Conclusions

A conceptual model of the interactions between a nighttime mesoscale katabatic flow on an extensive plain and a circular crater basin on the plain that is surrounded by an elevated rim has been developed using data from a steady-state period during the clear, synoptically undisturbed night of 26–27 October 2013. The conceptual model extended research conducted in the Meteor Crater in 2006 (Whiteman et al. 2010), which lacked upstream and rim wind and potential temperature profiles.

This research provides additional supporting data for features identified or postulated in the previous research, including the splitting of the approaching flow around the crater at low elevations, the lifting over the rim of cold stable air on the plain by the katabatic wind, the descent of the overflowing cold air into the crater until reaching its buoyancy equilibrium level, and the decreasing penetration depths with angular distance from the upwind crater rim.

The present paper adds further information on the depth and strength of the approaching katabatic flow and the stable layer on the plain that drives it, the dividing streamline that separates the air carried around the crater from the air carried over the crater rim, the depth and strength of the cold air imported over the crater rim, and the important role of the pre-existing temperature structure inside the crater on the cold air penetration. Additionally, a major flow feature, a bifurcation, is identified in which the lower negatively buoyant portion of the flow produces a cold air intrusion down the sidewall while the nonnegatively buoyant upper portion is carried quasi-horizontally over the crater. This bifurcation occurs over the rim, forming a relatively warm (in comparison with the background temperature structure inside the crater) neutral stability cavity or wake in the lee of the rim containing weak and variable direction winds. The cold air intrusion forms a hydraulic jump below the cavity.

The wealth of field data in the present experiments, the idealized shape of the crater basin, the steady katabatic flow on the adjacent plain, and the quiescent synoptic environment are expected to make this case study an ideal test case for numerical models that can be run in parametric studies to extend the results to other settings. The understanding gained in this idealized setting can be expected to be useful in understanding stably stratified overflows over other types of terrain into preexisting stably stratified downstream environments, whether in the atmosphere or in other fluids.

A separate research paper (Whiteman et al. 2018) investigates an IOP in which the cold-air intrusion was enhanced by stronger background winds to cause profound disturbances inside the crater including downslope-windstorm-type events associated with warm-air intrusions (Adler et al. 2012; Lehner et al. 2016b) strong enough to erode the crater floor cold pool.

Acknowledgments. Barringer Crater Corporation and Meteor Crater Enterprises are thanked for crater access, outstanding cooperation, and field assistance. Data were collected and processed by the National Center for Atmospheric Research's Earth Observing Laboratory (EOL), the University of Utah, and the Karlsruhe Institute of Technology (KIT). We appreciate the assistance of field personnel and organizations listed in Lehner et al.'s (2016b) acknowledgments. Matthew O. G. Hills is thanked for useful discussions. This research was supported by the National Science Foundation's Physical and Dynamic Meteorology Division through Grant AGS-1160730 (Whiteman). KIT was funded by the International Bureau of BMBF under Grant 01 DM 13002 (Kalthoff). We thank three anonymous reviewers for useful comments that improved this paper.

REFERENCES

Adler, B., C. D. Whiteman, S. W. Hoch, M. Lehner, and N. Kalthoff, 2012: Warm-air intrusions in Arizona's Meteor Crater. *J. Appl. Meteor. Climatol.*, **51**, 1010–1025, https://doi.org/10.1175/JAMC-D-11-0158.1.

Armi, L., and D. Farmer, 2002: Stratified flow over topography: Bifurcation fronts and transition to the uncontrolled state. *Proc. Roy. Soc. London*, **458A**, 513–538, https://doi.org/10.1098/rspa.2001.0887.

Baines, P. G., 1995: *Topographic Effects in Stratified Flows.* Cambridge University Press, 482 pp.

——, 1999: Downslope flows into a stratified environment—Structure and detrainment. *Mixing and Dispersion in Stably Stratified Flows*, P. A. Davies, Ed., Clarendon Press, 1–22.

Benjamin, T. B., 1962: Theory of the vortex breakdown phenomenon. *J. Fluid Mech.*, **14**, 593–629, https://doi.org/10.1017/S0022112062001482.

Cherukuru, N. W., R. Calhoun, M. Lehner, S. W. Hoch, and C. D. Whiteman, 2015: Instrument configuration for dual-Doppler lidar coplanar scans: METCRAX II. *J. Appl. Remote Sens.*, **9**, 096090, https://doi.org/10.1117/1.JRS.9.096090.

Doran, J. C., T. W. Horst, and C. D. Whiteman, 1990: The development and structure of nocturnal slope winds in a simple valley. *Bound.-Layer Meteor.*, **52**, 41–68, https://doi.org/10.1007/BF00123177.

Emanuel, K. A., and D. J. Raymond, 1993: *The Representation of Cumulus Convection in Numerical Models. Meteor. Monogr.*, No. 46, Amer. Meteor. Soc., 246 pp.

Grachev, A. A., L. S. Leo, S. Di Sabatino, H. J. S. Fernando, E. R. Pardyjak, and C. W. Fairall, 2016: Structure of turbulence in katabatic flows below and above the wind-speed maximum. *Bound.-Layer Meteor.*, **159**, 469–494, https://doi.org/10.1007/s10546-015-0034-8.

Grisogono, B., and D. Belušić, 2009: A review of recent advances in understanding the meso- and microscale properties of the severe Bora wind. *Tellus*, **61A**, 1–16, https://10.1111/j.1600-0870.2008.00369.x.

Haiden, T., and C. D. Whiteman, 2005: Katabatic flow mechanisms on a low-angle slope. *J. Appl. Meteor.*, **44**, 113–126, https://doi.org/10.1175/JAM-2182.1.

——, ——, S. W. Hoch, and M. Lehner, 2011: A mass flux model of nocturnal cold-air intrusions into a closed basin. *J. Appl. Meteor. Climatol.*, **50**, 933–943, https://doi.org/10.1175/2010JAMC2540.1.

Horst, T. W., and J. C. Doran, 1986: Nocturnal drainage flow on simple slopes. *Bound.-Layer Meteor.*, **34**, 263–286, https://doi.org/10.1007/BF00122382.

Kiefer, M. T., and S. Zhong, 2011: An idealized modeling study of nocturnal cooling processes inside a small enclosed basin. *J. Geophys. Res.*, **116**, D20127, https://doi.org/10.1029/2011JD016119.

Lehner, M., R. Rotunno, and C. D. Whiteman, 2016a: Flow regimes over a basin induced by upstream katabatic flows—An idealized modeling study. *J. Atmos. Sci.*, **73**, 3821–3842, https://doi.org/10.1175/JAS-D-16-0114.1.

——, and Coauthors, 2016b: The METCRAX II field experiment: A study of downslope windstorm-type flows in Arizona's Meteor Crater. *Bull. Amer. Meteor. Soc.*, **97**, 217–235, https://doi.org/10.1175/BAMS-D-14-00238.1.

Mahrt, L., and R. Heald, 2015: Common marginal cold pools. *J. Appl. Meteor. Climatol.*, **54**, 339–351, https://doi.org/10.1175/JAMC-D-14-0204.1.

Orr, A., G. J. Marshall, J. C. R. Hunt, J. Sommeria, C.-G. Wang, N. P. M. Van Lipzig, D. Cresswell, and J. C. King, 2008: Characteristics of summer airflow over the Antarctic Peninsula in response to recent strengthening of westerly circumpolar winds. *J. Atmos. Sci.*, **65**, 1396–1413, https://doi.org/10.1175/2007JAS2498.1.

Poulos, G., and S. Zhong, 2008: An observational history of small-scale katabatic winds in mid-latitudes. *Geogr. Compass*, **2**, 1798–1821, https://doi.org/10.1111/j.1749-8198.2008.00166.x.

Reinecke, P. A., and D. R. Durran, 2008: Estimating topographic blocking using a Froude number when the static stability is nonuniform. *J. Atmos. Sci.*, **65**, 1035–1048, https://doi.org/10.1175/2007JAS2100.1.

Renfrew, I. A., 2004: The dynamics of idealized katabatic flow over a moderate slope and ice shelf. *Quart. J. Roy. Meteor. Soc.*, **130**, 1023–1045, https://doi.org/10.1256/qj.03.24.

Rotunno, R., and M. Lehner, 2016: Two-layer stratified flow past a valley. *J. Atmos. Sci.*, **73**, 4065–4076, https://doi.org/10.1175/JAS-D-16-0132.1.

Savage, L. C., III, S. Zhong, W. Yao, W. J. O. Brown, T. W. Horst, and C. D. Whiteman, 2008: An observational and numerical study of a regional-scale downslope flow in northern Arizona. *J. Geophys. Res.*, **113**, D14114, https://doi.org/10.1029/2007JD009623.

Seemann, J., 1979: Agrotopoclimatology. *Agrometeorology*, J. Seemann et al., Eds., Springer, 125–130, https://doi.org/10.1007/978-3-642-67288-0_17.

Smith, R. B., 1989: Hydrostatic airflow over mountains. *Advances in Geophysics*, Vol. 31, Academic Press, 1–41, https://doi.org/10.1016/S0065-2687(08)60052-7.

Thorpe, S. A., 1998: Some dynamical effects of internal waves and the sloping sides of lakes. *Physical Processes in Lakes and Oceans*, J. Imberger, Ed., AGU Coastal and Estuarine Studies, Vol. 54, Amer. Geophys. Union, 441–460.

Vosper, S. B., I. P. Castro, W. H. Snyder, and S. D. Mobbs, 1999: Experimental studies of strongly stratified flow past three-dimensional orography. *J. Fluid Mech.*, **390**, 223–249, https://doi.org/10.1017/S0022112099005133.

Whiteman, C. D., and S. Zhong, 2008: Downslope flows on a low-angle slope and their interactions with valley inversions. Part I: Observations. *J. Appl. Meteor. Climatol.*, **47**, 2023–2038, https://doi.org/10.1175/2007JAMC1669.1.

——, J. M. Hubbe, and W. J. Shaw, 2000: Evaluation of an inexpensive temperature datalogger for meteorological applications. *J. Atmos. Oceanic Technol.*, **17**, 77–81, https://doi.org/10.1175/1520-0426(2000)017<0077:EOAITD>2.0.CO;2.

——, and Coauthors, 2008: METCRAX 2006: Meteorological experiments in Arizona's Meteor Crater. *Bull. Amer. Meteor. Soc.*, **89**, 1665–1680, https://doi.org/10.1175/2008BAMS2574.1.

——, S. W. Hoch, M. Lehner, and T. Haiden, 2010: Nocturnal cold-air intrusions into a closed basin: Observational evidence and conceptual model. *J. Appl. Meteor. Climatol.*, **49**, 1894–1905, https://doi.org/10.1175/2010JAMC2470.1.

——, and Coauthors, 2018: The nocturnal evolution of atmospheric structure in a basin as a larger-scale katabatic flow is lifted over its rim. *J. Appl. Meteor. Climatol.*, **57**, https://doi.org/10.1175/JAMC-D-17-0156.1, in press.

Winters, K. B., and L. Armi, 2014: Topographic control of stratified flows: Upstream jets, blocking and isolating layers. *J. Fluid Mech.*, **753**, 80–103, https://doi.org/10.1017/jfm.2014.363.

Zardi, D., and C. D. Whiteman, 2012: Diurnal mountain wind systems. *Mountain Weather Research and Forecasting*, F. K. Chow, S. F. J. De Wekker, and B. J. Snyder, Eds., Springer, 35–119.